Ion channel degeneracy enables robust and tunable neuronal firing rates

Guillaume Drion, Timothy O'Leary, Eve Marder

Biology Department and Volen Center

Brandeis University

Waltham, MA 02454

USA

Corresponding author: marder@brandeis.edu

Key words
FI Curve
Bifurcation
Type I excitability
Type II excitability
Reduced neuron model

Abstract

Firing rate is an important means of encoding information in the nervous system. To reliably encode a wide range of signals, neurons need to achieve a broad range of firing frequencies and to move smoothly between low and high firing rates. This can be achieved with specific ionic currents, such as A-type potassium currents, which can linearize the frequency-input current (FI) curve. By applying recently developed mathematical tools to a number of biophysical neuron models, we show how currents that are classically thought to permit low firing rates can paradoxically cause a jump to a high minimum firing rate when expressed at higher levels. Consequently, achieving and maintaining a low firing rate is surprisingly difficult and fragile in a biological context. This difficulty can be overcome via interactions between multiple currents, implying a need for ion channel degeneracy in the tuning of neuronal properties.

Significance Statement

Neurons need to be able to tune their firing rates to the input they receive. This requires a complex balance of different kinds of ion channels in the neuronal membrane and most neurons express many more kinds of ion channels than are strictly necessary to produce spikes. We apply recently developed analysis techniques to uncover a hidden fragility in the spiking properties of neurons. Achieving a smooth relationship between input and output in a neuron is more difficult than previously thought, but reliable spiking rates can be achieved using multiple ion channel types with overlapping, or degenerate properties. Our findings therefore suggest that biology exploits degeneracy to solve a difficult physiological tuning problem.

\body

Introduction

Firing rates encode the intensities of many signals in the nervous system, whether these are inputs from sensory organs, internal representations of percepts or muscle contraction commands in motor nerves. For a neuron to represent continuously varying signals in its firing rate, it must be able to fire at low, high and all intermediate frequencies. Experimentally, this means the frequency-input (or FI) curve has a specific shape, called Type I, such that firing frequency smoothly approaches zero at current threshold (1-6). By contrast, so-called Type II neurons have a lower bound in their firing frequency and move abruptly from quiescence to fast spiking, with this transition visible as a sharp jump in the FI curve at threshold (1, 3, 5).

Type I behavior is physiologically unlikely with a minimal set of membrane currents such as the voltage-gated sodium and delayed-rectifier potassium currents in the classical Hodgkin-Huxley model, which is Type II. Classic experimental (1, 7) and theoretical studies (3-5, 8, 9) revealed that a Type II membrane (such as a squid giant axon) can be turned into a Type I membrane by adding an inactivating (A-type) potassium conductance, I_A. As the density of I_A channels increases from zero, the membrane is able to support progressively lower firing frequencies at spiking threshold. The resulting 'linearization' of the FI curve from Type II to Type I has clear consequences for encoding information in firing rate as well as other computational properties such as thresholding and gain scaling, all of which are subjects of intense research (10-17).

We now show that this picture is incomplete. Using rigorous but intuitive methods (18) and building on previous technical results (19-21) we show that introducing I_A to a Type II neuron progressively linearizes but then de-linearizes the FI curve as I_A density increases further. Consequently I_A density must be tuned in a strict range to achieve Type I behavior. However, we show that other, unrelated currents including voltage gated calcium currents can produce the same transition from Type II to Type I behavior while having opposing effects on current threshold. Thus, tuning intrinsic neuronal properties while maintaining Type I behavior requires multiple membrane currents with degenerate properties.

Results

Type I excitability exists over a limited range of ion channel densities.

The classic 'linearizing' effect of I_A on a Type II FI curve is shown in Figure 1 (left and middle panels). FI curves were generated using the Connor-Stevens model (2, 3) with firing frequency measured at steady-state in response to current injection. The left panel in Figure 1 shows Type II behavior: as input current increases there is a sharp transition from no spiking to repetitive spiking at the current threshold. The middle panel of Figure 1 shows the classic result (2, 3) that adding an inactivating potassium conductance (I_A) smooths-out (or 'linearizes') the FI curve near current threshold, allowing the neuron to fire at arbitrarily low frequencies. However, increasing I_A further results in a transition back to a Type II-like FI curve, which we call Type II*, and where once again a sharp transition in firing frequency is observed at threshold (right panel of Figure 1). To the best of our knowledge, previous analyses have not documented nor explained this second transition.

This transformation from Type II to Type I is also seen under completely different circumstances, as shown in Figure 2A. Here we have used the same model neuron as in Figure 1 and compared the effects of adding the A-type conductance with the effects caused by adding a non-inactivating voltage-gated (L-type-like) calcium conductance (I_{Ca}).

There are notable similarities and differences between the effects of these two conductances on the original FI curve. First, we see that the two conductances induce opposite changes in the current threshold (Figure 2A, left panel). Current threshold increases as I_A conductance density increases, whereas increases in I_{Ca} result in progressively lower (hyperpolarized) current thresholds. This contrasting effect on current threshold is intuitive given the fact that I_A corresponds to an outward current, while I_{Ca} is inward. However, both conductances induce exactly the same sequence of transitions in FI curve shape, from Type II, to Type I and back to Type II-like (Type-II*) as conductance density increases. Importantly, the membrane potential waveforms at

comparable points in the FI curves are indistinguishable between the I_A and I_{Ca} cases (middle panel, Figure 2A).

Previous analyses have examined the IV curve of a neuron in the Type I and Type II regimes, showing that Type I neurons have a non-monotonic IV curve in voltage range near threshold. Type II neurons, by contrast, have a monotonic IV curve. This result is seen in Figure 2B: the IV curves where both g_A and g_{Ca} equal 0 mS cm^{-2} (Type II) are monotonically increasing, but become non-monotonic as the neuron switches to Type-I (g_A = 90 mS cm^{-2} or g_{Ca} = 0.4 mS cm^{-2}). However, monotonicity is not recovered for the transition to Type-II*, showing that the IV curve does not unambiguously determine Type-I behavior.

The task of relating the shape of an FI curve to the dynamics of individual conductances is complicated by the nonlinear nature of voltage-gated conductances, and a large literature on this problem exists (2, 5, 8, 9, 22-30). However, the observation that two completely different currents can induce qualitatively similar changes in FI curve shape suggests a general underlying mechanism. Furthermore, the fact that we observe the same sequence of transitions (Type II-Type I-Type II*) under different conditions suggests that the novel transition from Type I to Type II* might also belong to such a general mechanism.

Type I excitability requires voltage-insensitive transmembrane current at potentials just beneath threshold

To establish a general mechanistic understanding of the Type II-Type I-Type II* transitions, we exploited recent results that provide a general step-by-step algorithm for splitting the total membrane conductance in a neuron into components at different timescales (see methods and (18) for a full description of this procedure). The family of components is called the dynamic input conductance (DIC) (18) because it generalizes input conductance (as a function of membrane potential) to transient regimes. An important feature of the DIC framework is that conductances are split into a finite and manageable number of temporal components, typically three in total. These components account for physiologically relevant features in the membrane potential dynamics of a neuron. For example, the fastest component corresponds to the fastest gating event, generically the action potential upstroke. Each component has a quantifiable contribution from distinct ionic conductances such as I_A.

In Figure 3A we illustrate briefly the DIC analysis for currents during an action potential in the Connor-Stevens model. An action potential, or spike, has two inherent timescales. This fact was first appreciated by Hodgkin and Huxley (27) in the squid giant axon, where they identified a fast, regenerative inward current responsible for the spike upstroke and a slower 'delayed rectifying' current that helped to repolarize the membrane. In the case of the squid giant axon these currents are completely separable into sodium and potassium currents, but in general any single ionic conductance can contribute to multiple timescales and multiple ionic currents can contribute to any single timescale. DIC analysis captures these contributions in the form of compound membrane conductances with characteristic timescales.

Figure 3A (left panel) shows an action potential waveform and the underlying membrane currents. By definition, conductance is the derivative of current with respect to voltage, as indicated by the relation $\Delta I = -g\Delta V$. The two relevant components of the DIC for an action potential, the fastest component, g_f, ('f' for 'fast') and the next-fastest component, g_s ('s' for 'slow') are indicated on the respective membrane current traces. The sign, magnitude and voltage dependence of g_f and g_s account for the dynamics of a spike. In particular, the sign of the DIC curve determines whether it is restorative or regenerative, that is, whether it tends to provide negative or positive feedback, respectively, via membrane potential variations (8, 21, 22, 28).

For example, in the case of g_f, (Fig 3, right, red trace) there is a strong positive feedback as spiking threshold, V_{thr}, is exceeded. Positive deflections in membrane potential activate inward current, which further depolarizes the membrane, leading to the regenerative action potential upstroke. Similarly, at suprathreshold potentials, g_s (blue trace) contributes a strong negative feedback on membrane potential: the contribution comes from two processes, depolarization-induced inactivation of the inward sodium current and depolarization-induced activation of the outward potassium current. Thus, g_s repolarizes the membrane in the suprathreshold regime and has components from both sodium current inactivation and potassium (delayed rectifier) activation. It is important to emphasize the point that positive and negative feedback do not simply correspond to inward or outward current, what matters is how the conductance influences membrane potential and how, in turn, membrane potential

feeds back on the gating of the conductance (i.e. whether it leads to activation or inactivation).

Having understood the suprathreshold dynamics that generate spikes, we are now in a position to consider how the DIC curves influence the shape of the FI curve. In essence, the FI curve summarizes inter-spike dynamics because it is the inter-spike interval that sets firing frequency. Above threshold a spike is already taking place, so the only contribution that membrane potential dynamics make to firing frequency is via spike width. We therefore need to examine the DIC curves close to threshold voltage. If we zoom in on the peri-threshold regions of the DIC curves in Figure 3 (region labeled 'AHP' for after-hyperpolarization), we see the crucial feature that determines the Type I behavior: g_s, evaluated at V_{thr}, $g_s(V_{th})$, approaches zero as the FI curve transitions to Type I from either Type II or Type II* (Figure 3B). From this observation it is intuitively clear that 'pure Type I', which corresponds to an infinite interspike interval at V_{thr}, is bounded by two Type II-like regions. This fact turns out to be crucial in understanding why any change in conductance that causes a transition from Type II to Type I is generically followed by a transition back to a Type II-like FI curve. We provide a heuristic understanding of this transition in what follows, followed by a more rigorous phase plane analysis.

For a neuron to continuously fire at a low rate it must maintain an extremely small transmembrane depolarizing current during the interspike interval. This simple fact results from the membrane equation $C_m\, dV/dt = -I_m$ and the small magnitude of the current has been carefully characterized experimentally (31). Maintaining such a small current implies that voltage-dependence of the membrane conductance is relatively insensitive to the membrane potential variations occurring between two spikes. This sensitivity is characterized by the value of $g_s(V_{th})$.

In the absence of both I_A and I_{Ca}, $g_s(V_{th})$ is strictly negative (Fig 3B, dark blue curves). This means that the transmembrane current is restorative around threshold potential (g_s experiences negative feedback). In this case the depolarizing current flowing during the interspike interval decreases as the membrane potential depolarizes, mainly due to the activation of the delayed-rectifier potassium current. Regular spiking is therefore only achievable if the subthreshold depolarizing current is sufficiently large to be maintained during the whole interspike interval, which imposes

a minimum rate of membrane potential variation and thus a minimal firing frequency and a jump in the FI curve.

In the presence of a large density of either I_A or I_{Ca}, $g_s(V_{th})$ is positive (Fig 3B, green and red curves). This means that the transmembrane current is regenerative around threshold potential (g_s experiences positive feedback). In this case, the depolarizing current flowing during the interspike interval amplifies as the membrane potential depolarizes, due to the inactivation of I_A or the activation of I_{Ca}. As a result, an arbitrarily small depolarizing current cannot be maintained during the interspike interval, which again imposes a minimum rate of membrane potential variation, manifesting as a minimal firing frequency and as a jump in the FI curve.

The fact that both I_A and I_{Ca} can cause a transition from restorative (negative $g_s(V_{th})$) to regenerative (positive $g_s(V_{th})$) in the Connor-Stevens model deserves attention. I_A generates an outward current, whereas I_{Ca} is inward. However, the relevant gating variable of I_A in the Connor-Stevens model is the slow inactivation. Inactivation of an outward current that is itself activated by positive membrane potential deflections is a net positive feedback loop. On the other hand, I_{Ca} activates on a similar slow timescale and also promotes positive membrane potential deflections that further amplify the calcium conductance, which is also a positive feedback loop. Thus, due to the way their gating variables behave on the slow timescale, both I_A and I_{Ca} have equivalent effects on minimum firing frequency in spite of contributing opposite membrane currents.

Interspike interval only becomes unbounded as $g_s(V_{th})$ becomes very small, which only happens for intermediate values of either g_A or g_{Ca} (Fig 3B, light blue and purple curves). In this intermediate case, the regenerative effect of I_A or I_{Ca} balances the restorative effect of the delayed-rectifier potassium current around threshold potential. In turn, the transmembrane current is barely sensitive to membrane potential variations between two spikes, and an arbitrarily small current can be maintained throughout the whole interspike interval. This allows for an arbitrarily slow rate of membrane potential variation, corresponding to an arbitrarily low minimal firing frequency.

Type-I behaviour is therefore always a bounded region in parameter space flanked by two dynamical regimes, both of which are characterized by non-zero minimum firing

frequencies in an FI curve. This bounded region can be small and therefore fragile, as can be seen in Figure 3. For example, tuning g_{Ca} to achieve Type-I behaviour requires a tolerance of less than 0.4 mS/cm^2, whereas for I_A this region is 100 times larger in units of maximal conductance. Consequently for a neuron to achieve Type-I behavior it must carefully balance the expression of currents that strongly modulate g_s in order to remain in the Type-I regime. The sensitivity of Type-I behavior is observed experimentally and numerically: g_s and its associated membrane current must be small throughout the AHP region, and this is in fact seen in precise and difficult biophysical experiments (31) as well as detailed modeling studies (32). Furthermore, increasing I_A in the Type-II* regime of the Connor-Stevens model will only serve to exacerbate the jump to high minimum firing frequency and can never linearize the FI curve.

Hysteresis in the Type II* FI curve

There is a qualitative difference between the case where $g_s(V_{thr})$ is strictly negative (Type-II) and strictly positive (Type-II*). This difference manifests as hysteresis in the FI curve which can be revealed by the choice of stimulation protocol. Figure 4 shows two different FI curve protocols. A more traditional protocol (Fig 4A, left) starts from zero current and injects progressively higher amplitude depolarizing current steps, extracting the steady-state firing frequency for each step. For this protocol, no difference is observed in the qualitative shape of the FI curve between the Type-II and Type-II* regimes.

A difference between Type-II and Type-II* FI curves becomes apparent by adopting a non-standard FI curve protocol (Fig 4A, right). Starting with steady depolarizing current, this alternative protocol steps down toward zero current. This protocol reveals a lower minimum frequency in the right-hand family of FI curves where I_A density is high. The novel Type-II* regime is therefore accompanied by an additional dynamical feature: hysteresis in the FI curve. An important empirical message is that the choice of protocol (e.g. using the traditional protocol alone) can obviate important dynamical properties of a neuron in an experimental setting. Furthermore, hysteresis of this kind not only has relevance to how a neuron will interact in a circuit, it is also indicative of specific dynamical properties of the underlying conductances.

Tuning neuronal spiking properties requires ion channel degeneracy.

We have shown that several novel and perhaps counterintuitive relationships exist between FI curves and classically studied currents such as I_A. The DIC method, which is agnostic to the identity of underlying conductance that contributes to g_s, shows that completely unrelated currents (e.g. inward calcium currents) have dynamically equivalent effects on firing behavior. This has interesting consequences for strategies that neurons can use to tune excitable behavior.

Figure 5A shows how inclusion of both I_A and I_{Ca} in the Connor-Stevens model can allow some physiological properties of the neuron to be tuned while keeping others fixed. As we saw in Figure 2, both I_{Ca} and I_A can induce a Type-II-Type-I transition and thus are able to control the minimum firing rate of the neuron because they both contribute to $g_s(V_{th})$. In addition, the fact that I_A generates outward current while I_{Ca} generates inward current means that the two have opposing effects on the current threshold (Fig 2).

Figure 5A (top left) shows how current threshold varies as the two conductances are varied independently in the same model. There is a prominent region (solid black arrow) where current threshold is invariant, but the minimum firing frequency varies (Fig 5A, top right, solid black arrow). This path in parameter space defines a family of neurons with fixed current thresholds and variable firing frequencies, as visible in the FI curves measured at several points in this parameter space (Fig 5A, bottom left). Conversely, a neuron can keep minimum firing frequency fixed and vary current threshold by moving in a transverse direction in parameter space (Fig 5A, top panels, dashed black arrows).

The ability to independently tune current threshold and minimum firing frequency is critical for neurons that need to achieve specific firing activities. For instance, a neuron that requires spontaneous low frequency firing needs to balance ion channel densities to simultaneously achieve Type I excitability (small $g_s(V_{th})$) and set its transmembrane current close to current threshold ($I_{th} = 0$). Fig 5B illustrates this property in the Connor-Stevens model by showing in a parameterscape (33) how current threshold and minimum firing frequency co-vary as a function of g_A and g_{Ca}. The figure shows that most of the conductance values lead to non-zero current thresholds (colored outer circles), non-zero minimum firing frequencies (gray inner circles) or both. Spontaneous low frequency firing is solely possible for bounded, non-

zero values of both g_A and g_{Ca} (white region). The existence of such a region therefore relies on the fact that I_A and I_{Ca} have analogous effects on $g_s(V_{th})$ but opposite roles in determining overall transmembrane current.

Ion channels have paradoxical effects on excitability in different neuron types

The generality of the DIC analysis permits us to extract further unanticipated consequences of membrane currents that have been characterized in specific neurons in the literature. Figure 6 shows three completely different models, along with the Connor-Stevens model. Each model neuron has different kinds of I_A conductance and/or a voltage-gated calcium conductance. Remarkably, many of these conductances produce paradoxical effects that can be reconciled by DIC analysis. The middle column of Figure 6 (g_s sensitivity) shows how $g_s(V_{th})$ varies as the densities of the relevant conductances in the models are varied.

In the top row of Figure 6 we see the original result from Figure 1: both I_A and I_{Ca} produce a positive shift in $g_s(V_{th})$ (g_s sensitivity is positive for both currents) and thus move an existing Type-II membrane toward Type-I (FI curves, right column). The fact that I_{Ca} induces a shift to Type-I with only a small change in its maximal conductance is captured in the large magnitude of g_s sensitivity relative to that of I_A (roughly 200-fold).

By contrast, a crab STG motorneuron model (34), initially Type-II*, is brought back toward Type-I by increasing the density of the version of I_A. The calcium conductance in the STG model behaves the same way as that in the first example, pushing the FI curve further into Type-II* behavior and resulting in a larger FI curve hysteresis. Thus, the STG model contains an I_A conductance that has the opposite effect to the Connor-Stevens I_A and the signature of this difference is seen in negative g_s sensitivity.

Paradoxical effects are seen between different I_A conductance types in the same model. This depends on whether activation or inactivation of the A-type conductance dominates g_s at V_{thr}, which in turn depends on the specific kinetics of the I_A subtype and the other conductances present in the cell. Figure 6 (third row) shows a dorsal cochlear nucleus neuron model (35) with two subtypes of I_A conductance, $I_{A,1}$ and $I_{A,2}$. Owing to differences in their kinetics, the sensitivity of g_s to these two conductances is opposite in sign. As a consequence, a Type-II membrane in the control condition is

moved toward Type-I by $I_{A,1}$ and further into the Type-II regime by $I_{A,2}$. Finally, a ventral cochlear nucleus neuron model (36, 37) again has two different I_A conductances, but neither has positive g_s sensitivity. Thus the control FI curve, which is Type-II, cannot be linearized toward Type I by either of its A-type potassium conductances.

Connection to classical phase plane analysis

Previous work relies on planar reductions of conductance-based models to analyze dynamics in a phase plane (4, 5, 8, 24, 25, 28, 38-41). Our approach here is quite different and, we hope, more intuitive to physiologists who think about neuronal dynamics in terms of contributions of voltage-dependent ionic current at different timescales. However, it is important to frame our results using a classical phase plane analysis so that connections can be made to the broadest body of work.

We performed a standard reduction of the Connor Stevens model of Figure 1, using the method of (42) to express all the slow 'recovery' variables in terms of a single slow variable, w (methods). Figure 7 shows the three regimes (Type II, Type I and Type II*) in the reduced model, with their respective phase planes plotted at current threshold.

We see the same qualitative shifts in the FI curve in the reduced model as $\bar{g}_A$ is increased (Figure 7A), although due to the approximate nature of the planar reduction, the transitions between the three types of FI curves occur at different numerical values of $\bar{g}_A$ as compared with the full model.

The phase plane allows us to show the type of bifurcation responsible for the onset of spiking in each case (Figure 7B). At low $\bar{g}_A$, Type II firing (Figure 7, left) occurs due to an Andronov-Hopf bifurcation at a critical value of applied current, I_{Hopf}, as is widely known from previous analyses (5, 8, 19, 20, 24, 25, 28, 42, 43).

As $\bar{g}_A$ is increased, a lower branch of the V-nullcline gradually appears (Figure 7B, middle and right panels), forming an 'hourglass' shape that differs strikingly from the familiar 'inverted N' seen in most planar reductions. The emergence of a lower branch was observed in a previous reduction of the Connor-Stevens model using the method of equivalent potentials (39), although the physiological meaning of this branch remained in question until very recent work (19-21) which used singularity theory to prove its

existence. The lower branch corresponds to the addition of a positive feedback component in the slow timescale, which coexists with the negative feedback in the single recovery variable, w. The existence of a lower V-nullcline branche turns out to be crucial for understanding Type I and Type II* behavior.

In the Type I case (Figure 7B, middle panel) the upper and lower V-nullcline branches kiss at the onset of spiking when $\bar{g}_A$ is at a critical value (approximately 25 mS/cm^2 in the reduced model). For values of $\bar{g}_A$ close to this critical value, the proximity of the two branches creates a bottleneck in dV/dt (Figure 7A, middle panel insets) leading to slow spiking characteristic of a Type I membrane. Spiking occurs through a Saddle Node on Invariant Circle (SNIC) bifurcation, as reported in the literature (5, 8, 28). The insets of Figure 7B, middle panel, shows the SNIC bifurcation as $g_s(V_{th})$ approaches zero from either side (the case $g_s(V_{th}) = 0$ is shown in the main panel). When $g_s(V_{th}) \lesssim 0$ the saddle-node occurs on the upper branch of the V-nullcline; when $g_s(V_{th}) \gtrsim 0$ the saddle-node is on the lower branch. At $g_s(V_{th}) = 0$ a saddle-node occurs when the lower and upper branches of the V-nullcline meet at the intersection with the w-nullcline. In all three cases, the trajectory is confined to pass through the saddle-node (the criterion for a SNIC), permitting long interspike intervals. Furthermore, we see that the region of parameter space that can sustain the SNIC bifurcation and Type-I excitability is finite in extent (as opposed to a single point).

Increasing $\bar{g}_A$ further leads to a situation where the onset of spiking occurs due to a Saddle-Node/Saddle-Homoclinic bifurcation. The saddle-node bifurcation occurs on the lower V-nullcline branch long before it approaches the upper branch (Figure 7B, right). As in the low-$\bar{g}_A$/Type II case, there is no bottleneck to slow down dV/dt arbitrarily, resulting in a lower bound in spiking frequency and a Type II-like FI curve. Note that SNIC has indeed been shown to produce Type II behavior (44). However, onset and termination of spiking occur at two different bifurcations (Saddle Node and Saddle Homoclinic respectively), resulting in hysteresis in the FI curve. This hysteresis is much larger and robust than the one related to the subcritical Hopf bifurcation at $\bar{g}_A = 0$ (21) such that only the former is observed in the experimental protocol of Figure 4.

We can bridge the DIC and phase-plane viewpoints of Type I excitability by computing $g_s(V_{thr})$ in the reduced model. By definition g_s is the derivative of the slow current with

respect to membrane potential (18), which is easily computed in the planar reduction because the slow timescale dynamics depend on a single variable, w:

$$g_s = \frac{\partial \dot{V}}{\partial w}\frac{\partial w_\infty}{\partial V} \qquad (1)$$

From our previous analyses, we have a criterion for Type I excitability, namely $g_s(V_{th}) \approx 0$. Examining the terms on the right-hand side of equation (1), this implies either the slope of the w nullcline is almost zero at V_{th} ($\partial w_\infty / \partial V \approx 0$) or that the derivative of membrane current with respect to the slow gating variable is around zero at V_{th} ($\partial \dot{V} / \partial w \approx 0$). From the phase planes in Figure 7B we see that the former case is not possible in the Connor Stevens model because the bifurcation occurs at a steep point of the w nullcline. Thus, the condition for the SNIC bifurcation differs from the canonical account, which typically shows a SNIC bifurcation occurring in the flat region of the slow recovery variable (see, for example (5)).

Our present analysis therefore illustrates a subtle but important point: the SNIC bifurcation responsible for Type-I excitability can occur via multiple mechanisms and the canonical mechanism may not be representative of all neurons. In particular, any transition to Type I from Type II that is caused by a change in maximal conductances alone can only affect the first term on the right hand side of Equation (1) and is therefore likely to occur via the V-nullcline bottleneck mechanism described in Figure 7B as opposed to the canonical mechanism.

Discussion

A key step in understanding neuronal membrane potential dynamics is finding a way to isolate and characterize the contributions of the many different ionic conductances present in a typical neuron. In spite of the power of conductance-based models for understanding neurophysiology, a clear picture of how individual conductances contribute to features that are physiologically meaningful, such as spiking threshold and minimum firing frequency, can be difficult to achieve. In this work we leverage recently developed theoretical tools to show that a classic result in neurophysiology has a hidden and significant component that is missing from previous work.

I_A is classically thought to linearize an FI curve from Type-II to Type-I. The implications of this transition for circuit function are widely appreciated. However, as we have

shown here, the original model that reproduces this transition has a previously undescribed transition from Type-I back to Type-II-like behavior (Type-II*). We also showed how this transition can be readily understood in terms of components of a summary quantity, the dynamic input conductance (18). Furthermore, the analysis provides a route to identifying this second transition empirically, by modifying an FI curve protocol to uncover hysteresis.

An important feature of the DIC analysis is its generality. The identity of a membrane conductance, including whether it is inward or outward, does not fully determine a specific physiological phenomena, such as the transition from Type-II to Type-I. Thus an inward (calcium) current is able to induce the same transitions as an outward current like I_A. This allows neurons to compensate or tune physiologically relevant features of neuronal firing, such as current threshold and minimum firing frequency. Interestingly, as revealed in Figure 5, these kinds of features can be tuned while keeping other features fixed if maximal conductances are co-varied along approximately linear paths in parameter space. This provides a link to recent experimental observations (45-47) and theoretical models of activity-dependent ion channel regulation (48, 49) in which linear correlations between conductance densities are seen.

DIC analysis also reveals and explains paradoxical effects of membrane conductance models in the literature. For example, as we saw in Figure 6, not all I_A currents in the literature exert the same effect on firing properties of neurons. Depending on their kinetic properties and the model in which they are implemented, A-type currents are capable of inducing opposite effects on the shape of an FI curve. This fact does not challenge the traditional view that I_A linearizes FI curves, but rather, it adds nuance: I_A currents that exert a specific positive shift in the slow component of the DIC at threshold can induce a transition from Type-II to Type-I. Some, but not all I_A currents fit into this class.

Type I behavior is difficult to achieve with a minimal set of membrane currents such as the voltage-gated sodium and delayed-rectifier potassium currents in the classical Hodgkin-Huxley model (27), whereas Type II behavior is easier to achieve. Nonetheless, Type I behavior is essential in neural circuits that encode information in firing rate (14), or in situations where slow pacemaking is important physiologically

(32, 50). The fact that Type-I is a bounded, and sometimes small region in parameter space presents a potential regulation problem for a neuron that has only a few different membrane currents. Tuning membrane conductances to achieve Type I behavior can be made easier if a neuron expresses many kinds of ion channel that all contribute to g_s. It therefore seems more than a coincidence that there is an abundance of subtypes of A-type channels in many, if not most, nervous system genomes (51-53).

Together, these results point to a clear role for degeneracy in the regulation of intrinsic neuronal properties: while a minimal set of channel types is sufficient in principle, fine tuning their expression to achieve precise firing behavior might be biologically unfeasible in practice. On the other hand, a larger palette of currents with some differing properties as well as some overlapping properties makes specific behaviors more accessible and robust.

Methods

Connor-Stevens model

Model equations are described in (3). Briefly, the model is composed of a leak current I_{leak}, a transient sodium current I_{Na}, a delayed-rectifier potassium current I_{Kd} and a transient A-type potassium current I_A. In addition, we added non-inactivating calcium current I_{Ca} of the form

$$I_{Ca} = \bar{g}_{Ca}\, m_{Ca}^2\, (V - V_{Ca})$$

where

$$\frac{dm_{Ca}}{dt} = \frac{m_{Ca,\infty}(V) - m_{Ca}}{\tau_{m_{Ca}}}$$

$$m_{Ca,\infty}(V) = \frac{1}{1 + \exp(-0.15(V + 50))}\ ;\ \tau_{m_{Ca}} = 2.35\ ms$$

Parameters used in simulations are as follows: $C_m = 1\ \mu F/cm^2$, $V_{Na} = 55\ mV$, $V_K = -75\ mV$, $V_{Ca} = 120\ mV$, $V_{leak} = -17\ mV$; $\bar{g}_{Na} = 120\ mS/cm^2$, $\bar{g}_{Kd} = 20\ mS/cm^2$, $\bar{g}_{leak} = 0.3\ mS/cm^2$, $\bar{g}_A \in [0, 210]\ mS/cm^2$ and $\bar{g}_{Ca} \in [0, 1]\ mS/cm^2$. $\bar{g}_A$ and $\bar{g}_{Ca}$ are never present simultaneously, with the exception of Fig. 5.

The values of the current steps shown in Fig. 1 are $I_{step,1} = 2\ \mu A/cm^2$ (black trace) and $I_{step,2} = 6\ \mu A/cm^2$ (blue trace) in the three cases ($\bar{g}_{Ca} = 0\ mS/cm^2$). Initial applied currents are $I_{app} = -12\ \mu A/cm^2$ for $\bar{g}_A = 0\ mS/cm^2$, $I_{app} = 20\ \mu A/cm^2$ for $\bar{g}_A = 90\ mS/cm^2$ and $I_{app} = 60\ \mu A/cm^2$ for $\bar{g}_A = 180\ mS/cm^2$. The step responses shown in Fig. 4A are for $\bar{g}_A = 210\ mS/cm^2$ (current values are depicted on the figure).

The FI curves shown in Fig. 1, Fig. 2A and Fig. 4B, left are computed using steps of $0.1\ \mu A/cm^2$ of applied current and the initial condition $V_0 = -65\ mV$, all other variables being initially set at their steady-state value ($m_0 = m_\infty(V_0)$, …). The FI curves shown in Fig. 4B, right are computed similarly using the initial condition $V_0 = -25\ mV$.

The IV curves shown in Fig. 2B correspond to the membrane equation with all variables set at their steady-state values ($m = m_\infty(V)$, …). The different IV curves are shifted vertically to achieve similar resting potentials for the three values of $\bar{g}_A$ (Fig. 2B, left) or $\bar{g}_{Ca}$ (Fig. 2B, right).

Dynamic input conductances (DICs) in all cases are computed using the method described in (18) using two timescales (fast and slow).

In Fig 3 the fast timescale, τ_f, corresponds to the sodium activation time constant $\tau_f(V) = \tau_{mNa}(V)$ and the slow timescale, τ_s, corresponds to the potassium activation time constant $\tau_s(V) = \tau_{mKd}(V)$. The threshold potential V_{th} is estimated to be $-50\,mV$.

Plots showing the relationship between the minimum frequency and the value of the slow dynamic input conductance at spike threshold, $g_s(V_{th})$, (Fig. 3B, right) are generated for values of $\bar{g}_A$ ranging from $0\,mS/cm^2$ to $210\,mS/cm^2$ by steps of $2\,mS/cm^2$, or for values of $\bar{g}_{Ca}$ ranging from $0\,mS/cm^2$ to $1\,mS/cm^2$ by steps of $0.01\,mS/cm^2$. The minimum frequency is extracted using steps of $0.001\,\mu A/cm^2$ of applied current and the initial condition $V_0 = -65\,mV$, all other variables being initially set at their steady-state value. The diagram shown in Fig. 4D is computed similarly using the two initial conditions $V_0 = -65\,mV$ and $V_0 = -25\,mV$. The value of $g_s(V_{th})$ is computed for each case as described above.

Parameter maps shown at the top of Fig. 5A and Fig. 5B are computed as above by independently varying $\bar{g}_A$ and $\bar{g}_{Ca}$. $\bar{g}_A$ ranges from $0\,mS/cm^2$ to $60\,mS/cm^2$ in steps of $2\,mS/cm^2$, and $\bar{g}_{Ca}$ ranges from $0\,mS/cm^2$ to $0.5\,mS/cm^2$ in steps of $0.02\,mS/cm^2$.

Reduced Connor-Stevens model

We reduced the Connor-Stevens model following the method described in (42). Sodium channel activation and A-type potassium channel activation are merged in the fast timescale ($m_{Na} = m_{Na,\infty}(V)$ and $m_A = m_{A,\infty}(V)$). Delayed-rectifier potassium channel activation, sodium channel inactivation and A-type potassium channel inactivation variables are merged into a single slow variable w ($m_{Kd} = w$, $h_{Na} = h_{Na,\infty}(w_\infty^{-1}(w))$, $h_A = h_{A,\infty}(w_\infty^{-1}(w))$). We set $w_\infty(V) \equiv m_{Kd,\infty}(V)$. Because $m_{Kd,\infty}(V)$ is not invertible in closed form in the original CS model, we use the exponential fit

$$m_{Kd,\infty}(V) = \frac{1}{1.05 + \exp(-0.065(41.6 + V))}$$

which gives

$$m_{Kd,\infty}^{-1}(V) = -(200\log(1/V - 21/20))/13 - 208/5$$

Parameters for the phase portraits of Fig. 7, bottom are $\bar{g}_A = 0\ mS/cm^2$ and $I_{app} = -9.81\ \mu A/cm^2$ (left), $\bar{g}_A = 25\ mS/cm^2$ and $I_{app} = -1.09\ \mu A/cm^2$ (center), and $\bar{g}_A = 0\ mS/cm^2$ and $I_{app} = 8.66\ \mu A/cm^2$ (right). All other parameters are as described in the full model.

STG neuron model

Full model equations are described in (34). Briefly, the model is composed of a leak current I_{leak}, a transient sodium current I_{Na}, a delayed-rectifier potassium current I_{Kd}, a transient A-type potassium current I_A, two high-threshold transient calcium currents $I_{Ca,T}$ and $I_{Ca,S}$ and voltage-gated calcium-activated potassium current $I_{K,Ca}$. Parameters used in simulations are as follows: $C_m = 0.628\ \mu F/cm^2$, $V_{Na} = 60\ mV$, $V_K = -80\ mV$, $V_{Ca} = 80\ mV$, $V_{leak} = -50\ mV$; $\bar{g}_{Na} = 900\ mS/cm^2$, $\bar{g}_{Kd} = 90\ mS/cm^2$, $\bar{g}_{leak} = 0.01\ mS/cm^2$, $\bar{g}_{Ca,S} = 0\ mS/cm^2$, $\bar{g}_{K,Ca} = 0\ mS/cm^2$, $\bar{g}_{Ca,T} = 0.8\ or\ 1.2\ mS/cm^2$ and $\bar{g}_A = 0\ or\ 40\ mS/cm^2$. The threshold potential V_{th} is estimated around $-50\ mV$.

g_s sensitivity is computed by taking the derivative of the slow dynamic input conductance at spike threshold over the A-type potassium current maximal conductance ($\frac{\partial g_s(V_{th})}{\partial \bar{g}_A}$) or over the transient calcium current maximal conductance ($\frac{\partial g_s(V_{th})}{\partial \bar{g}_{Ca,T}}$) as appropriate. DIC timescales are chosen as follows: $\tau_f(V) = \tau_{m_{Na}}(V)$, $\tau_s(V) = \tau_{m_{Kd}}(V)$ and $\tau_u(V) = \tau_{h_{Ca,S}}(V)$.

FI curves are computed using steps of $0.01\ \mu A/cm^2$ of applied current. Initial conditions are $V_0 = -60\ mV$ and $V_0 = -30\ mV$, with all other variables set to their steady-state value. The values of the conductances in each case are $\bar{g}_{Ca,T} = 0.8\ mS/cm^2$ and $\bar{g}_A = 0\ mS/cm^2$ (black curve), $\bar{g}_{Ca,T} = 0.8\ mS/cm^2$ and $\bar{g}_A = 40\ mS/cm^2$ (blue curve) and $\bar{g}_{Ca,T} = 1.2\ mS/cm^2$ and $\bar{g}_A = 0\ mS/cm^2$ (orange curve).

DCN neuron model

Model equations are described in (35). Briefly, the model is composed of a leak current I_{leak}, a transient sodium current I_{Na}, a non-inactivating potassium current I_{KNI}, two inactivating potassium current I_{KIF} (called $I_{A,1}$ in the present paper) and I_{KIS} (called $I_{A,2}$ in the present paper), and a hyperpolarization-activated cation current I_H. Parameters used in simulations are as follows: $C_m = 12.5\,pF$, $V_{Na} = 50\,mV$, $V_K = -81.5\,mV$, $V_H = -43\,mV$, $V_{leak} = -57.7\,mV$; $\bar{g}_{Na} = 350\,nS$, $\bar{g}_{KNI} = 80\,nS$, $\bar{g}_{leak} = 2.8\,nS$, $\bar{g}_H = 3\,nS$, $\bar{g}_{KIS} = 40\ or\ 60\,nS$ and $\bar{g}_{KIF} = 150\ or\ 600\,nS$. The threshold potential V_{th} is estimated to be $-50\,mV$.

g_s sensitivity is computed by taking the derivative of the slow dynamic input conductance at spike threshold with respect to the fast-inactivating potassium current maximal conductance ($\frac{\partial g_s(V_{th})}{\partial \bar{g}_{A,1}}$) and with respect to the slowly inactivating potassium current maximal conductance ($\frac{\partial g_s(V_{th})}{\partial \bar{g}_{A,2}}$) in each case. DIC timescales are chosen as follows: $\tau_f(V) = \tau_{m_{Na}}(V)$, $\tau_s(V) = \tau_{m_{KNI}}(V)$ and $\tau_u(V) = \tau_{h_{KIS}}(V)$.

The FI curves are computed using steps of $1\,pA$ of applied current and the initial condition $V_0 = -50\,mV$, all other variables being initially set at their steady-state value. The values of the conductances in each case are $\bar{g}_{KIS} = 40\,mS/cm^2$ and $\bar{g}_{KIF} = 150\,mS/cm^2$ (black curve), $\bar{g}_{KIS} = 40\,mS/cm^2$ and $\bar{g}_{KIF} = 600\,mS/cm^2$ (blue curve) and $\bar{g}_{KIS} = 60\,mS/cm^2$ and $\bar{g}_{KIF} = 150\,mS/cm^2$ (orange curve).

VCN neuron model

Model and equations are described in (36). The model is composed of a leak current I_{leak}, a transient sodium current I_{Na}, a low-treshold potassium current I_{LT} (called $I_{A,2}$ in the present paper), a high-treshold potassium current I_{HT}, a transient A-type potassium current I_A (called $I_{A,1}$ in the present paper), and an hyperpolarization-activated cation current I_H. Parameters used in simulations are as follows: $C_m = 12\,pF$, $V_{Na} = 55\,mV$, $V_K = -70\,mV$, $V_H = -43\,mV$, $V_{leak} = -65\,mV$; $\bar{g}_{Na} = 1000\,nS$, $\bar{g}_{HT} = 0\,nS$, $\bar{g}_{leak} = 2\,nS$, $\bar{g}_H = 0.5\,nS$, $\bar{g}_{LT} = 0\ or\ 3\,nS$ and $\bar{g}_A = 200\ or\ 400\,nS$. The threshold potential V_{th} is estimated around $-50\,mV$.

g_s sensitivity is computed by taking the derivative of the slow dynamic input conductance at spike threshold with respect to the A-type potassium maximal conductance ($\frac{\partial g_s(V_{th})}{\partial \bar{g}_{A,1}}$) or the low-threshold potassium maximal conductance ($\frac{\partial g_s(V_{th})}{\partial \bar{g}_{A,2}}$) as appropriate. DIC timescales are chosen as follows: $\tau_f(V) = \tau_{m_{Na}}(V)$, $\tau_s(V) = \tau_{m_{HT}}(V)$ and $\tau_u(V) = \tau_{m_H}(V)$.

FI curves are computed using steps of $0.1\ pA$ of applied current and the initial condition $V_0 = -50\ mV$, all other variables being initially set at their steady-state value. The values of the conductances in each case are $\bar{g}_{LT} = 0\ mS/cm^2$ and $\bar{g}_A = 200\ mS/cm^2$ (black curve), $\bar{g}_{LT} = 0\ mS/cm^2$ and $\bar{g}_A = 400\ mS/cm^2$ (blue curve) and $\bar{g}_{LT} = 3\ mS/cm^2$ and $\bar{g}_A = 200\ mS/cm^2$ (orange curve).

Acknowledgments

Funding was provided by NIH PO1 NS 079149 and the Charles A. King Trust (TOL). GD is a Marie-Curie COFUND postdoctoral fellow at the University of Liege. Co-funded by the European Union. The authors acknowledge constructive discussions with Bruce Bean (Harvard University, USA), Alessio Franci (UNAM, Mexico), Julijana Gjorgieva (Brandeis University, USA) and members of the Marder lab.

References

1. Connor JA (1975) Neural repetitive firing: a comparative study of membrane properties of crustacean walking leg axons. *J Neurophysiol* 38(4):922-932.
2. Connor JA & Stevens CF (1971) Prediction of repetitive firing behaviour from voltage clamp data on an isolated neurone soma. *J Physiol* 213(1):31-53.
3. Connor JA, Walter D, & McKown R (1977) Neural repetitive firing: modifications of the Hodgkin-Huxley axon suggested by experimental results from crustacean axons. *Biophysical Journal* 18(1):81-102.
4. Ermentrout B (1996) Type I membranes, phase resetting curves, and synchrony. *Neural Computation* 8(5):979-1001.
5. Rinzel J & Ermentrout GB (1989) Analysis of neural excitability and oscillations. *Methods in neuronal modeling: From synapses to networks* (MIT Press) pp 135-169.
6. Hodgkin AL (1948) The local electric changes associated with repetitive action in a non-medullated axon. *J Physiol* 107(2):165-181.
7. Connor JA & Stevens CF (1971) Inward and delayed outward membrane currents in isolated neural somata under voltage clamp. *J Physiol* 213(1):1-19.
8. Prescott SA, De Koninck Y, & Sejnowski TJ (2008) Biophysical basis for three distinct dynamical mechanisms of action potential initiation. *Plos Comput Biol* 4(10) DOI: 10.1371/journal.pcbi.1000198
9. Rush ME & Rinzel J (1995) The potassium A-current, low firing rates and rebound excitation in Hodgkin-Huxley models. *Bull Math Biol* 57(6):899-929.
10. Herz AV, Gollisch T, Machens CK, & Jaeger D (2006) Modeling single-neuron dynamics and computations: a balance of detail and abstraction. *Science* 314(5796):80-85.
11. Koch C (1997) Computation and the single neuron. *Nature* 385(6613):207-210.
12. Olsen SR, Bortone DS, Adesnik H, & Scanziani M (2012) Gain control by layer six in cortical circuits of vision. *Nature* 483(7387):47-52.
13. Schwartz O & Simoncelli EP (2001) Natural signal statistics and sensory gain control. *Nature Neuroscience* 4(8):819-825.
14. Ratte S, Hong S, De Schutter E, & Prescott SA (2013) Impact of neuronal properties on network coding: roles of spike initiation dynamics and robust synchrony transfer. *Neuron* 78(5):758-772.
15. Brenner N, Bialek W, & de Ruyter van Steveninck R (2000) Adaptive rescaling maximizes information transmission. *Neuron* 26(3):695-702.
16. Fairhall AL, Lewen GD, Bialek W, & de Ruyter Van Steveninck RR (2001) Efficiency and ambiguity in an adaptive neural code. *Nature* 412(6849):787-792.
17. Gjorgjieva J, Mease RA, Moody WJ, & Fairhall AL (2014) Intrinsic neuronal properties switch the mode of information transmission in networks. *Plos Comput Biol* 10(12) DOI: 10.1371/journal.pcbi.1003962.
18. Drion G, Franci A, Dethier J, & Sepulchre R (2015) Dynamic Input Conductances Shape Neuronal Spiking. *eNeuro* 2(2) ENEURO.0031-14.2015
19. Drion G, Franci A, Seutin V, & Sepulchre R (2012) A Novel Phase Portrait for Neuronal Excitability. *Plos One* 7(8) DOI: 10.1371/journal.pone.0041806
20. Franci A, Drion G, & Sepulchre R (2012) An Organizing Center in a Planar Model of Neuronal Excitability. *Siam J Appl Dyn Syst* 11(4):1698-1722.
21. Franci A, Drion G, Seutin V, & Sepulchre R (2013) A Balance Equation Determines a Switch in Neuronal Excitability. *Plos Computational Biology* 9(5) DOI: 10.1371/journal.pcbi.1003040

22. Barreiro AK, Thilo EL, & Shea-Brown E (2012) A-current and type I/type II transition determine collective spiking from common input. *J Neurophysiol* 108(6):1631-1645.
23. Connor JA (1978) Slow repetitive activity from fast conductance changes in neurons. *Fed Proc* 37(8):2139-2145.
24. Ermentrout B (1998) Linearization of F-I curves by adaptation. *Neural Computation* 10(7):1721-1729.
25. Fitzhugh R (1960) Thresholds and plateaus in the Hodgkin-Huxley nerve equations. *J Gen Physiol* 43:867-896.
26. Ghigliazza RM & Holmes P (2004) Minimal Models of Bursting Neurons: How Multiple Currents, Conductances, and Timescales Affect Bifurcation Diagrams. *Siam J Appl Dyn Syst* 3(4):636-670.
27. Hodgkin AL & Huxley AF (1952) A quantitative description of membrane current and its application to conduction and excitation in nerve. *J Physiol* 117(4):500-544.
28. Izhikevich EM (2000) Neural excitability, spiking and bursting. *International Journal of Bifurcation and Chaos* 10(6):1171-1266.
29. Lundstrom BN, Famulare M, Sorensen LB, Spain WJ, & Fairhall AL (2009) Sensitivity of firing rate to input fluctuations depends on time scale separation between fast and slow variables in single neurons. *J Comput Neurosci* 27(2):277-290.
30. Meng X, Lu Q, & Rinzel J (2011) Control of firing patterns by two transient potassium currents: leading spike, latency, bistability. *J Comput Neurosci* 31(1):117-136.
31. Khaliq ZM & Bean BP (2008) Dynamic, nonlinear feedback regulation of slow pacemaking by A-type potassium current in ventral tegmental area neurons. *J Neurosci* 28(43):10905-10917.
32. Kuznetsova AY, Huertas MA, Kuznetsov AS, Paladini CA, & Canavier CC (2010) Regulation of firing frequency in a computational model of a midbrain dopaminergic neuron. *J Comput Neurosci* 28(3):389-403.
33. Gutierrez GJ, O'Leary T, & Marder E (2013) Multiple mechanisms switch an electrically coupled, synaptically inhibited neuron between competing rhythmic oscillators. *Neuron* 77(5):845-858.
34. Goldman MS, Golowasch J, Marder E, & Abbott LF (2001) Global structure, robustness, and modulation of neuronal models. *J Neurosci* 21(14):5229-5238.
35. Kanold PO & Manis PB (2001) A physiologically based model of discharge pattern regulation by transient K+ currents in cochlear nucleus pyramidal cells. *J Neurophysiol* 85(2):523-538.
36. Rothman JS & Manis PB (2003) The roles potassium currents play in regulating the electrical activity of ventral cochlear nucleus neurons. *J Neurophysiol* 89(6):3097-3113.
37. Rothman JS & Manis PB (2003) Differential expression of three distinct potassium currents in the ventral cochlear nucleus. *J Neurophysiol* 89(6):3070-3082.
38. Hindmarsh JL & Rose RM (1982) A model of the nerve impulse using two first-order differential equations. *Nature* 296(5853):162-164.
39. Kepler T, Abbott LF, Marder E (1991) Order reduction for dynamical systems describing the behavior of complex neurons. *Advances in neural information processing systems* 3:55-61
40. Kepler TB, Abbott LF, & Marder E (1992) Reduction of conductance-based neuron models. *Biological Cybernetics* 66(5):381-387.
41. Ratte S, Lankarany M, Rho YA, Patterson A, & Prescott SA (2014) Subthreshold membrane currents confer distinct tuning properties that enable neurons to encode the integral or derivative of their input. *Frontiers in cellular neuroscience* 8:452.

42. Franci A DG, Sepulchre R (2014) Modeling the modulation of neuronal bursting: a singularity theory approach. *Siam J Appl Dyn Syst* 13(2):798-829.
43. FitzHugh R (1955) Mathematical models of threshold phenomena in the nerve membrane. *Bulletin of Mathematical Biology* 17(4):257-278.
44. Izhikevich EM (2007) Dynamical Systems in Neuroscience: The Geometry of Excitability and Bursting. MIT Press.
45. Schulz DJ, Goaillard JM, & Marder EE (2007) Quantitative expression profiling of identified neurons reveals cell-specific constraints on highly variable levels of gene expression. *Proc Natl Acad Sci U S A* 104(32):13187-13191.
46. Temporal S, Lett KM, & Schulz DJ (2014) Activity-dependent feedback regulates correlated ion channel mRNA levels in single identified motor neurons. *Current biology* 24(16):1899-1904.
47. Ratte S, Zhu Y, Lee KY, & Prescott SA (2014) Criticality and degeneracy in injury-induced changes in primary afferent excitability and the implications for neuropathic pain. *eLife* 3:e02370.
48. O'Leary T, Williams AH, Caplan JS, & Marder E (2013) Correlations in ion channel expression emerge from homeostatic tuning rules. *Proc Natl Acad Sci U S A* 110(28):E2645-2654.
49. O'Leary T, Williams AH, Franci A, & Marder E (2014) Cell types, network homeostasis, and pathological compensation from a biologically plausible ion channel expression model. *Neuron* 82(4):809-821.
50. Tucker KR, Huertas MA, Horn JP, Canavier CC, & Levitan ES (2012) Pacemaker rate and depolarization block in nigral dopamine neurons: a somatic sodium channel balancing act. *J Neurosci* 32(42):14519-14531.
51. Carrasquillo Y & Nerbonne JM (2014) IA channels: diverse regulatory mechanisms. *The Neuroscientist* 20(2):104-111.
52. Coetzee WA*, et al.* (1999) Molecular diversity of K+ channels. *Ann New York Acad Sci* 868:233-285.
53. Jan LY & Jan YN (2012) Voltage-gated potassium channels and the diversity of electrical signalling. *J Physiol* 590(Pt 11):2591-2599.

Figure Legends

Fig 1. Increasing A-type potassium channel density in the Connor-Stevens model switches neuron excitability from Type II to Type I back to Type II*. The three panels show simulation results of the Connor-Stevens model for different values of A-type potassium channel density (from left to right: $\bar{g}_A$=0 mS/cm^2, $\bar{g}_A$=90 mS/cm^2 and $\bar{g}_A$=180 mS/cm^2, respectively). The top of each panel shows membrane potential traces (Vm) for two different step input currents (I_{app}) (black and blue traces). The bottom of each pannel shows neuron firing rate as a function of the input current (FI curve). Black points on the FI curves correspond to each of the example traces shown above.

Fig 2. Increasing A-type potassium current or L-type calcium current in the Connor-Stevens model has similar effects on the shape of the FI curve, but opposite effects on the current threshold. **A**. Left, FI curves of the Connor-Stevens model for different values of $\bar{g}_A$ ($\bar{g}_{Ca}$ = 0 mS/cm^2). Right, FI curves of the same Connor-Stevens model for different values of $\bar{g}_{Ca}$ ($\bar{g}_A$ = 0 mS/cm^2). Specific values of the current densities are depicted above each curve. Center, membrane potential variations over time at a similar frequency in the absence of both $\bar{g}_A$ and $\bar{g}_{Ca}$ (dark blue trace), for increasing values of $\bar{g}_A$ (light blue and green traces), and for increasing values of $\bar{g}_{Ca}$ (magenta and red traces). **B**. IV curves of the Connor-Stevens model for different values of $\bar{g}_A$ (left) and different values of $\bar{g}_{Ca}$ (right). Specific values of the current densities are depicted on each curve.

Fig 3. Neuron minimal firing frequency (f0) is shaped by the value of the slow dynamic input conductance at spike threshold. A. Left, membrane potential variations (top) and corresponding transmembrane current variations (bottom) over time in the Connor-Stevens model for $\bar{g}_A$=0 and $\bar{g}_{Ca}$=0. The red trace corresponds to the fast-varying current, the blue trace to the slowly varying current. Right, fast (red trace) and slow (blue trace) dynamic input conductances of the same model in the same configuration. **B**. Left, zoom of the slow dynamic input conductance (g_s) in the perithreshold region for different values of $\bar{g}_A$ (top) or different values of $\bar{g}_{Ca}$ (bottom). The dots depict the value of g_s at spike threshold in the different cases. Right, minimum firing frequency as a function of $g_s(V_{th})$ for increased $\bar{g}_A$ (top) or increased $\bar{g}_{Ca}$ (bottom). Colored points correspond to example traces in the left figure.

Fig 4. Increasing A-type potassium channel density in the Connor-Stevens model induces a robust hysteresis in the FI curve. A. Membrane potential traces (Vm) for four different step input currents (Iapp) using a step-up protocol (left) or a step-down protocol (right) ($\bar{g}_A$ = 210 mS/cm^2). B. FI curves of the Connor-Stevens model for different values of $\bar{g}_A$ as measured using increasing steps (left) or decreasing steps of applied current (right). Black arrows highlight the differences in current threshold measured with increasing vs decreasing steps. C. Merging of the FI curves shown in B. D. Minimum firing frequency as a function of the value of g_s at spike threshold for increased $\bar{g}_A$ when the two protocols are used. The hysteretic region is depicted in light gray.

Fig 5. A-type potassium channels and calcium channels correlate to independently tune current threshold and minimum firing rate in the Connor-Stevens model. A. Top, values of current threshold (left) and minimum firing frequency (right) in the Connor-Stevens model for different values of $\bar{g}_A$ and $\bar{g}_{Ca}$. Bottom, FI curves of the Connor-Stevens model for different couples of values for $\bar{g}_A$ and $\bar{g}_{Ca}$, each being depicted by dots of the corresponding color in the parameter charts. **B.** Parameterscape of current threshold and minimum firing rate as a function of $\bar{g}_A$ and $\bar{g}_{Ca}$ (top) and membrane potential variations over time for three sets of parameters (bottom).

Fig 6. Experimentally characterized currents have diverse and sometimes paradoxical effects on FI curves in specific neuron types. Each row depicts one of four different model neurons with experimentally characterized membrane currents, as described in the corresponding citation. For each model, the currents contributing to $g_s(V_{thr})$ are indicated in the first column, and the sensitivity (derivative) of $g_s(V_{thr})$ with respect to the density of each current is computed (second column). The third column shows FI curves of the different models in control condition (black trace) or after an increase in the density of one or the other current type (blue and orange traces).

Fig 7. Phase plane analysis of Type II-Type I-Type II* transitions in a two dimensional reduction of the Connor Stevens model. A. FI curves in a two-dimensional reduced Connor Stevens model (see methods) for three different values of $\bar{g}_A$ corresponding to Type II, Type I and Type II* (left to right, respectively). Bifurcation types are indicated at the respective values of the applied current (Hopf = Andronov-Hopf; SNIC = Saddle-Node on Invariant Circle; SN = Saddle-Node; SH = Saddle-Homoclinic). Stars indicate the value of the applied current at which each phase plane is plotted. **B.** Phase planes computed at spiking threshold for each of the three $\bar{g}_A$ cases. The specific bifurcation induced by applied current, I_{app}, is indicated on each plot (I_{Hopf} = Andronov-Hopf bifurcation; I_{SNIC} = Saddle-Node on Invariant Circle; I_{SN} = Saddle-Node). Open circles correspond to unstable fixed points, black filled circles to

stable fixed points and half-filled circles to saddle-node points. V-nullclines are shown in blue, while w-nullclines are shown in green. Insets: phase plane detail during repetitive spiking; red dotted arrows indicate membrane potential trajectories.

Figure 1

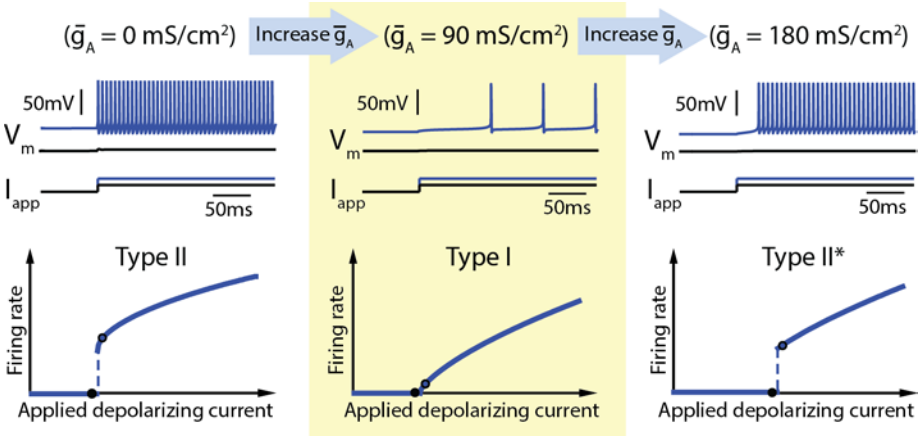

Figure 2

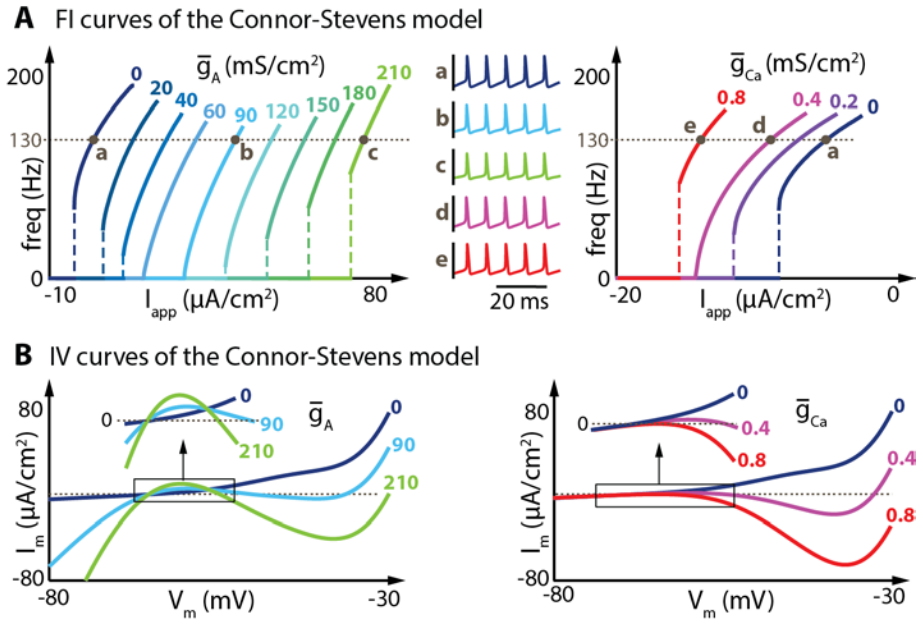

Figure 3

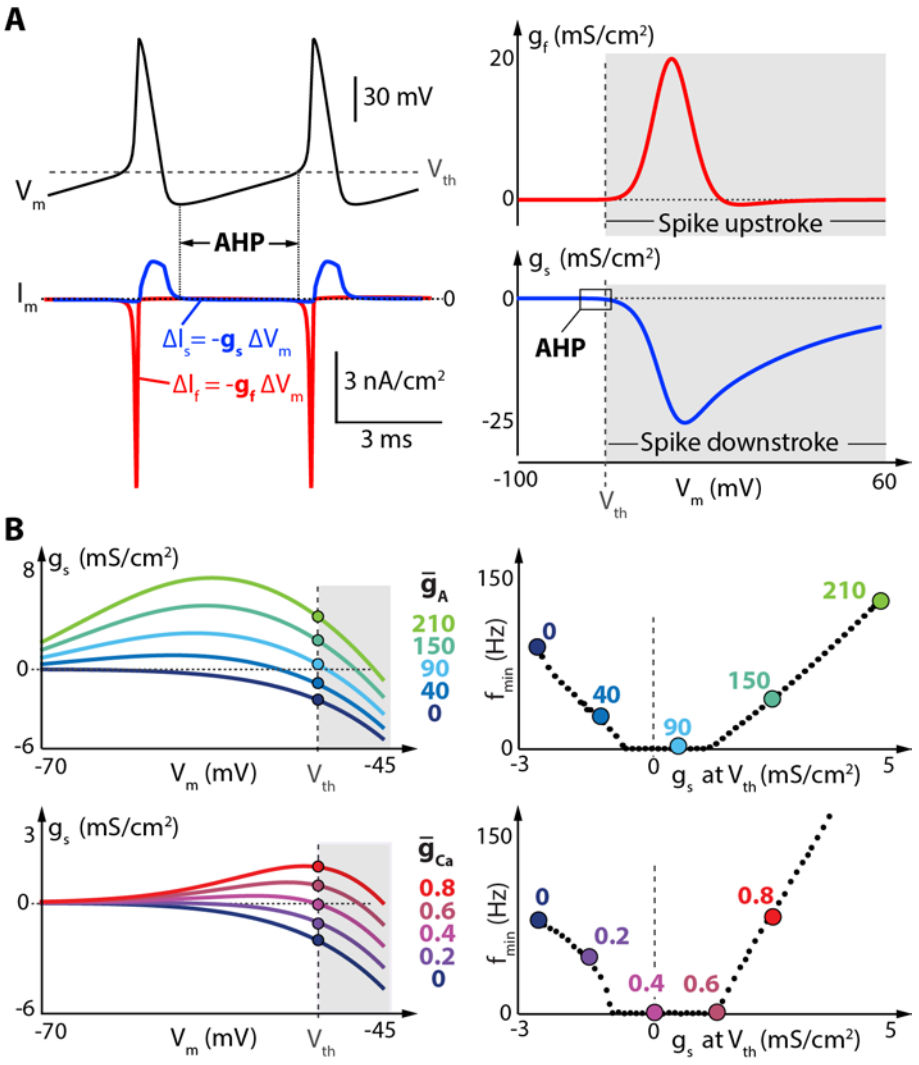
A
30 mV
V_m
V_th
AHP
I_m
0
ΔI_s = -g_s ΔV_m
ΔI_f = -g_f ΔV_m
3 nA/cm²
3 ms
g_f (mS/cm²)
20
0
Spike upstroke
g_s (mS/cm²)
0
AHP
-25
Spike downstroke
-100
V_m (mV)
60
V_th
B
g_s (mS/cm²)
8
0
-6
-70
V_m (mV)
V_th
-45
ḡ_A
210
150
90
40
0
150
f_min (Hz)
0
-3
g_s at V_th (mS/cm²)
5
g_s (mS/cm²)
3
0
-6
ḡ_Ca
0.8
0.6
0.4
0.2
0

Figure 4

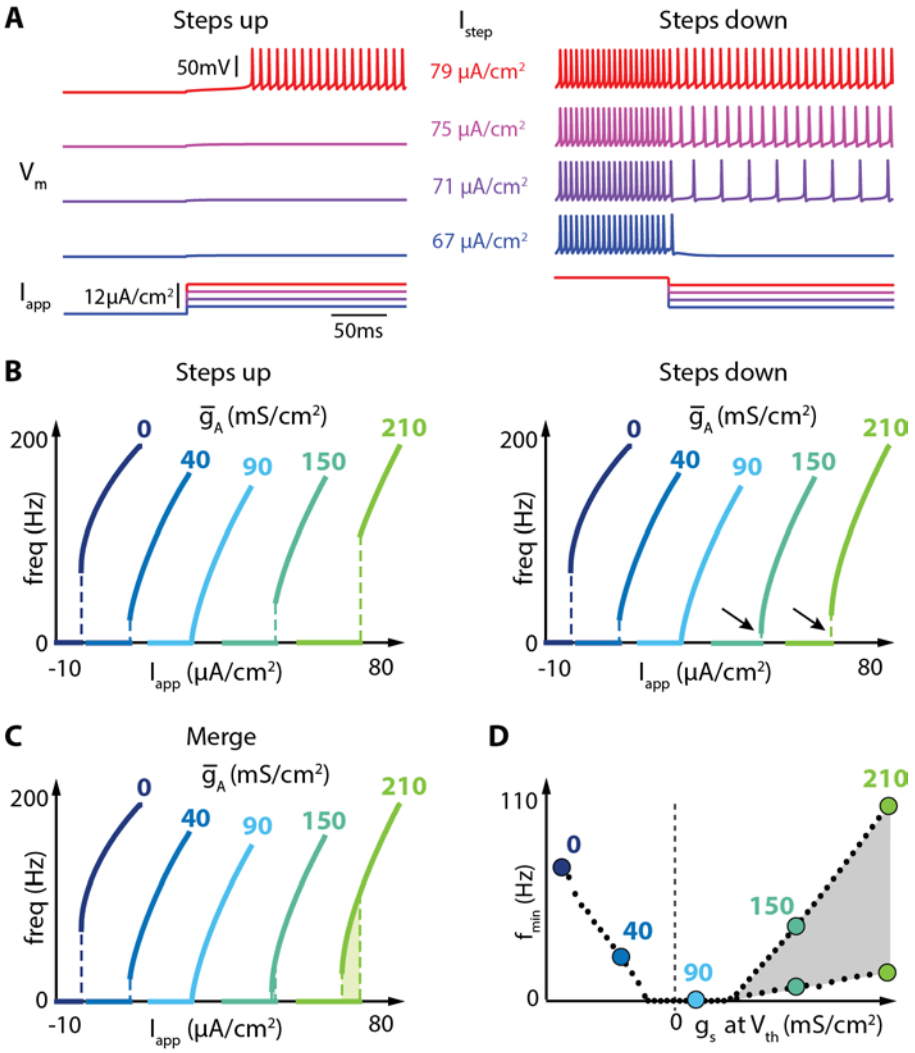
A
Steps up
I step
Steps down
50mV
79 µA/cm²
75 µA/cm²
V m
71 µA/cm²
67 µA/cm²
I app
12µA/cm²
50ms
B
Steps up
Steps down
ḡA (mS/cm²)
0
40
90
150
210
200
freq (Hz)
0
-10
I app (µA/cm²)
80
C
Merge
D
110
f min (Hz)
0 g s at V th (mS/cm²)

Figure 5

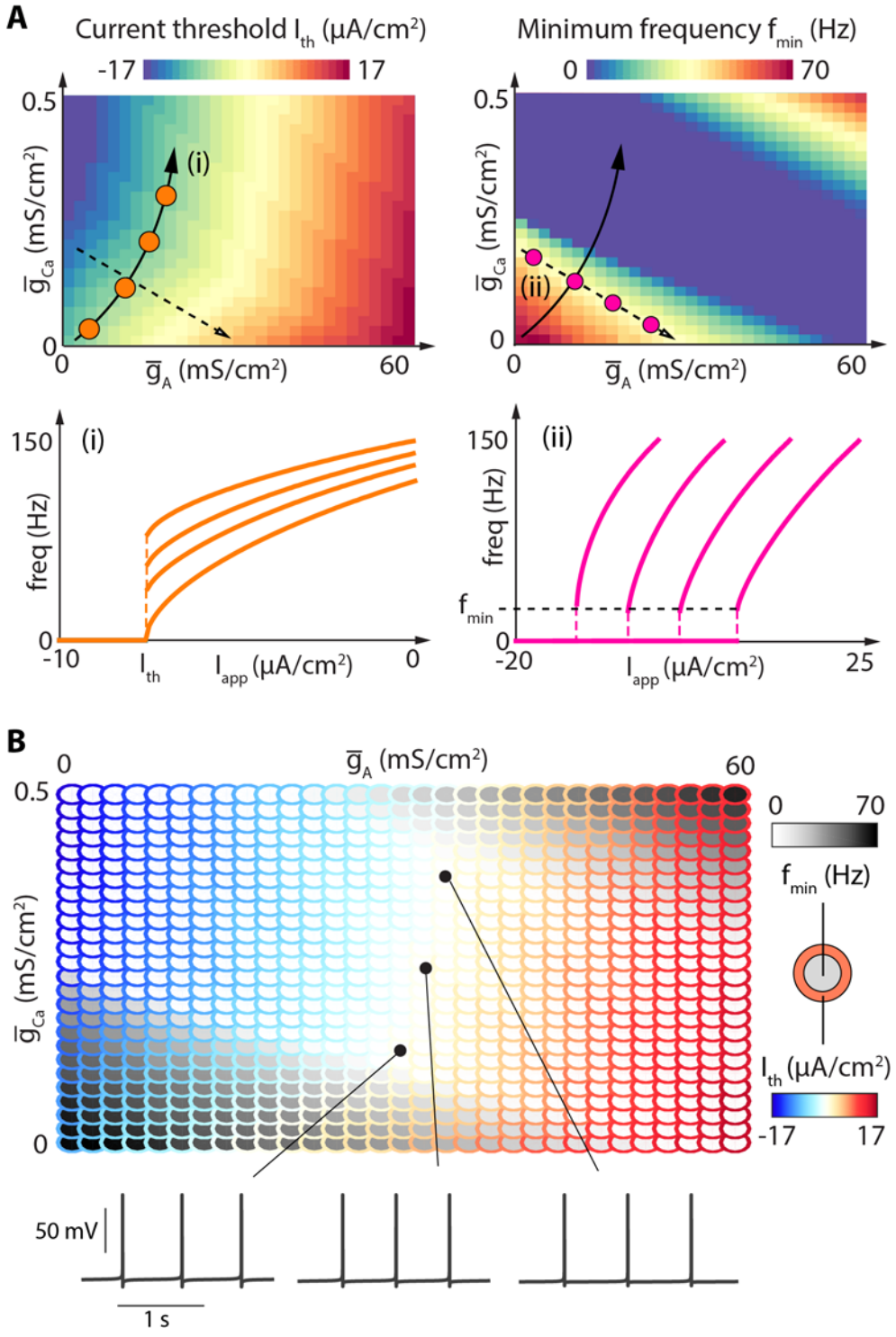
A
Current threshold I_{th} (μA/cm²)
-17
17
Minimum frequency f_{min} (Hz)
0
70
0.5
$\bar{g}_{Ca}$ (mS/cm²)
0
$\bar{g}_A$ (mS/cm²)
60
(i)
(ii)
150
freq (Hz)
f_{min}
-10
I_{th}
I_{app} (μA/cm²)
-20
25
B
50 mV
1 s

Figure 6

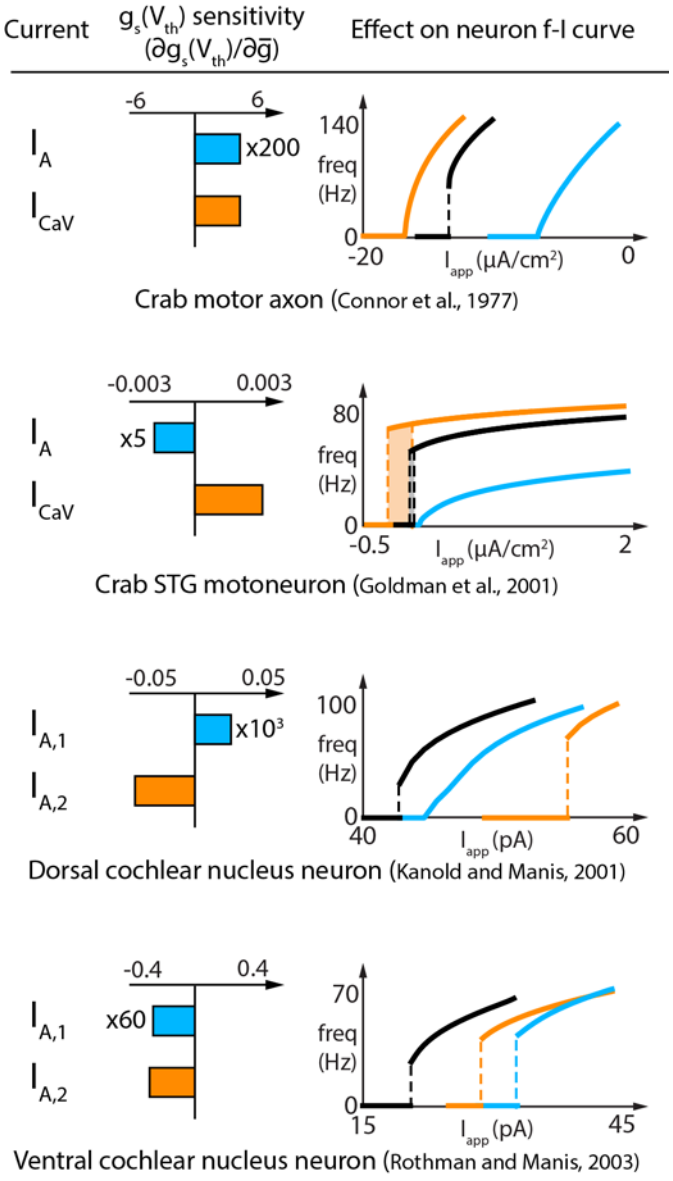
Current
$g_s(V_{th})$ sensitivity
$(\partial g_s(V_{th})/\partial \bar{g})$
Effect on neuron f-I curve
-6
6
I_A
I_{CaV}
x200
140
freq
(Hz)
0
-20
I_{app} (μA/cm²)
0
Crab motor axon (Connor et al., 1977)
-0.003
0.003
I_A
I_{CaV}
x5
80
freq
(Hz)
0
-0.5
I_{app} (μA/cm²)
2
Crab STG motoneuron (Goldman et al., 2001)
-0.05
0.05
$I_{A,1}$
$I_{A,2}$
x10³
100
freq
(Hz)
0
40
I_{app} (pA)
60
Dorsal cochlear nucleus neuron (Kanold and Manis, 2001)
-0.4
0.4
$I_{A,1}$
$I_{A,2}$
x60
70
freq
(Hz)
0
15
I_{app} (pA)
45
Ventral cochlear nucleus neuron (Rothman and Manis, 2003)

Figure 7

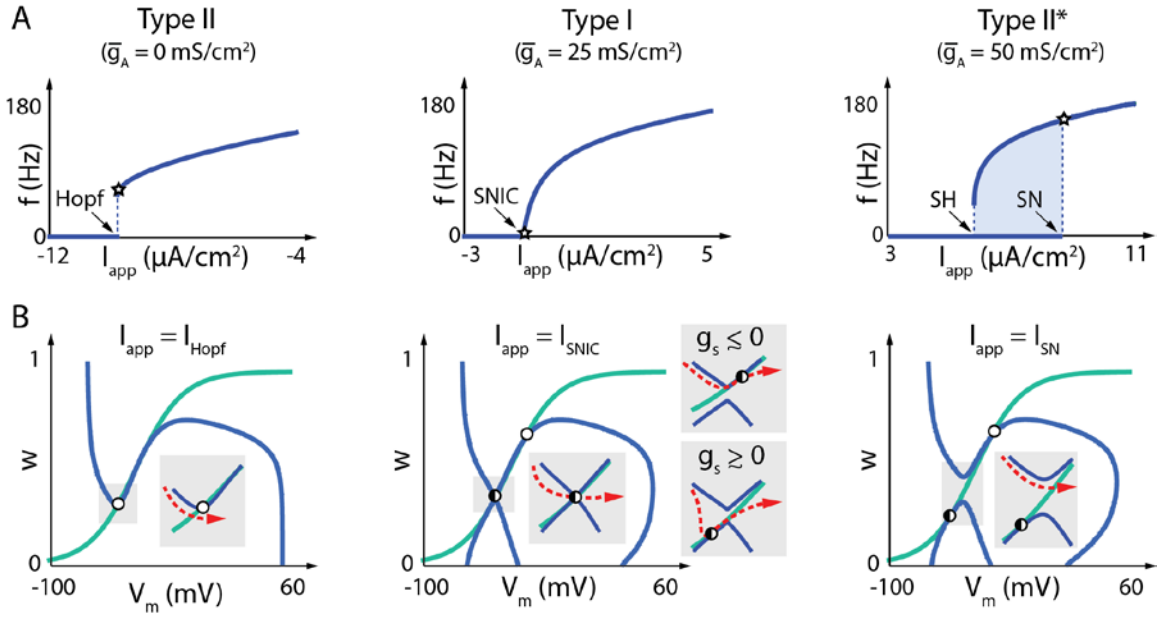
A
Type II
($\bar{g}_A$ = 0 mS/cm²)
Type I
($\bar{g}_A$ = 25 mS/cm²)
Type II*
($\bar{g}_A$ = 50 mS/cm²)
180
f (Hz)
0
Hopf
SNIC
SH
SN
-12
-4
-3
5
3
11
I_{app} (μA/cm²)
B
$I_{app} = I_{Hopf}$
$I_{app} = I_{SNIC}$
$I_{app} = I_{SN}$
$g_s \lesssim 0$
$g_s \gtrsim 0$
1
w
-100
60
V_m (mV)